IRNSS/NavIC Single-Point Positioning: A Service Area Precision Analysis

Safoora Zaminpardaz*, Peter J.G. Teunissen, and Nandakumaran Nadarajah

GNSS Research Centre, Curtin University, Perth, Australia
Email*: safoora.zaminpardaz@postgrad.curtin.edu.au

The Indian Regional Navigation Satellite System (IRNSS) has recently (May 2016) become operational. The system has been developed with the objective of offering positioning, navigation and timing (PNT) to the users in its two service areas, covering the Indian landmass and the Indian Ocean respectively. It is the goal of this contribution to provide further insight into the full-constellation L5 pseudorange single-point positioning (SPP) capabilities of the system. A detailed dilution of precision (DOP) analysis of its two service areas, including the identification, in location and time, of poor receiver-satellite geometries is provided. It is hereby demonstrated how the impact of some of these poor receiver-satellite geometries can be mitigated by means of height-constraining. An overview and analysis of the SPP precision is also provided including easy-to-use representative day-averaged values for a grid of locations covering the two service areas.

Keywords: Indian Regional Navigation Satellite System (IRNSS); Navigation with Indian Constellation (NavIC); Dilution of Precision (DOP); L5 Pseudorange; Single-Point Positioning (SPP)

1 Introduction

The Indian Regional Navigation Satellite System (IRNSS) has recently (May 2016) become operational and provided with the operational name of NavIC (Navigation with Indian Constellation). It has been developed by the Indian Space Research Organization (ISRO) with the objective of offering positioning, navigation and timing (PNT) to the users in its service area. It thereby provides two types of services: a standard positioning service (SPS) for civilian users and a restricted service (RS) for authorized users (ISRO 2014).

As IRNSS has recently become fully operational, it is important to gain an understanding of its navigational potential and actual positioning capabilities for civilian users. This is not only of general interest, but also specifically for users operating in its service area. There are to date only a few published studies on IRNSS's positioning performance and none were based on the full constellation. Among the published IRNSS studies, several are simulation-based (Mozo Garcia et al. 2010, Sarma et al. 2010, Sekar et al. 2012, Rethika et al. 2013, Rao 2013, Su et al. 2012), while some are based on real data, such as Thoelert et al. (2014) in which the clock stability of IRNSS-1A is assessed. The accuracy of a precise model for solar radiation pressure is tested using the IRNSS-1A and 1B observations in (Kumari et al. 2015). Babu et al. (2015) compares orbit determination methods for IRNSS-1A, 1B and 1C. In order to validate the orbit accuracy with modernized ephemeris parameters, Chandrasekhar et al. (2015) employs the IRNSS-1A, 1B and 1C real data. Montenbruck and Steigenberger (2015) used the observations of the IRNSS-1A and 1B to investigate the quality of the IRNSS navigation messages. Nadarajah et al. (2015), after assessing the IRNSS noise characteristics, combines the L5/E5 signals of IRNSS, GPS, Galileo and QZSS for instantaneous attitude determination. Some positioning results over India based on the 4-satellite data of I1, I2, I3, and I4 are presented in (Ganeshan et al. 2015, Pal and Ganeshan 2015), and the position accuracy of two IRNSS satellites integrated with the other satellite systems is presented in (Thombre et al. 2016). Zaminpardaz et al. 2016 presents the first IRNSS standalone positioning results over Australia and Odijk et al. (2016) presents the first analysis of the differential inter-system biases (DISBs) between L5 signal of IRNSS w.r.t. the L5/E5a signals of GPS, Galileo and QZSS.

The goals of this contribution are to provide insight into IRNSS and to demonstrate its full-constellation single-point positioning (SPP) performance. As such this contribution provides the first IRNSS standalone positioning performance analysis for different locations in its two service areas.

This contribution is organized as follows. In section 2 the full IRNSS constellation with its two service areas are described as well as the SPP model that forms the basis of our analyses. Section 3 provides a detailed dilution of precision (DOP) analysis of IRNSS's two service areas, including the identification, in location and time, of poor receiver-satellite geometries. It is hereby also demonstrated how the impact of some of these poor receiver-satellite geometries can be mitigated by means of height-constraining. An overview and analysis of the SPP precision for a grid of locations over the two service areas is given in section 4. It includes easy-to-use representative day-averaged values of the positioning precision.

2 The IRNSS/NavIC System

In this section we describe the IRNSS constellation with its two service areas as well as the single-point positioning (SPP) model that forms the basis of our analyses.

The IRNSS Constellation

The IRNSS constellation consists of three geostationary orbit (GEO) satellites and four inclined geosynchronous orbit (IGSO) satellites (see Figure 1 and Table 1). The orbital period of the IRNSS satellites is one sidereal day (23 hours and 56 minutes), such that the IRNSS satellite ground tracks repeat every solar day (24 hours) four minutes earlier. The IRNSS satellites transmit navigation signals, based on Code Division Multiple Access (CDMA), on L5 (1176.45 MHz) and on S (2492.028 MHz), with a Binary Phase-Shift Key (BPSK (1)) modulation for standard positioning service (SPS) users, and with a Binary Offset Carrier (BOC (5,2)) modulation for restricted service (RS) users (ISRO 2014).

The IRNSS is established with the objective of offering positioning, navigation and timing (PNT) services to the users in its service area. The IRNSS classifies its service areas broadly into the two regions shown in Figure 2. The primary service area of IRNSS encompasses the Indian landmass and a region lying within a distance of 1500 km from its geo-political boundary, and the secondary service area extends between latitudes 30° S to 50° N and longitudes 30° E to 130° E (Sarma et al. 2010, Ganeshan 2012, Saikiran and Vikram 2013). Also the secondary service area is important as it covers the Indian Ocean being one of the busiest oceans. The Indian Ocean is the third largest of the world's oceanic divisions, covering approximately 20% of the water on the Earth's surface. It contains major sea routes connecting the Middle East, Africa, and East Asia with Europe and the Americas, and it provides an estimated 40% of the world's offshore oil production.

The Single-Epoch SPP Model

We assume that a single receiver r is tracking m IRNSS satellites on frequency L5. The single-epoch, single-frequency linearized SPP observation equations can then be formulated in vector-matrix form as

$$\begin{aligned} E\{\Delta p_r\} &= [G_r \quad e_m]\begin{bmatrix} \Delta x_r \\ dt_r \end{bmatrix} \\ D\{\Delta p_r\} &= \sigma^2\, W_r^{-1} \end{aligned} \tag{1}$$

where $E\{.\}$ and $D\{.\}$ denote the expectation and dispersion operators, respectively. The m-vector Δp_r contains the observed-minus-computed pseudorange observables to the m IRNSS satellites. They are a priori corrected for the ionospheric delays and for the dry tropospheric delays.

The $m \times 3$ matrix $G_r = [-u_r^1, \ldots, -u_r^m]^T$ contains the unit direction vectors u_r^s, $s = 1, \ldots, m$, from the receiver antenna to the m tracked IRNSS satellites and e_m is the m-vector of ones. The 3-vector Δx_r is the receiver position increment, and the scalar dt_r is the increment of the receiver clock error biased by the receiver code hardware delay.

The parameter σ denotes the zenith-referenced user range accuracy which captures the observables noise characteristics as well as the remaining unmodeled effects. The $m \times m$ diagonal weight matrix $W_r = \mathrm{diag}\,(w_r^1, \ldots, w_r^m)$ contains the elevation-dependent weights (Euler and Goad 1991),

$$w_r^s = [1 + 10 \exp(-\frac{\varepsilon_r^s}{10})]^{-2} \tag{2}$$

with ε_r^s being the elevation of the satellite s with respect to receiver r.

Assuming that the design matrix $[G_r, e_m]$ is of full rank, the SPP weighted least-squares solution of the position vector is given as

$$\begin{aligned} \Delta\hat{x}_r &= (G_r^T W_D G_r)^{-1} G_r^T W_D \Delta p_r \\ Q_{\hat{x}_r \hat{x}_r} &= \sigma^2 (G_r^T W_D G_r)^{-1} \end{aligned} \tag{3}$$

in which $W_D = D_m (D_m^T W_r^{-1} D_m)^{-1} D_m^T$ and the range space of the $m \times (m-1)$ difference matrix D_m spans the orthogonal complement of e_m, i.e. $D_m^T e_m = 0$. By making use of the matrix identity $W_D = W_r\,(I_m - e_m (e_m^T W_r e_m)^{-1} e_m^T\, W_r)$, the variance matrix of $\Delta\hat{x}_r$ can also be expressed as

$$Q_{\hat{x}_r \hat{x}_r} = \sigma^2\, (\sum_{s=1}^{m} w_r^s\, [u_r^s - \bar{u}_r][u_r^s - \bar{u}_r]^T)^{-1} \tag{4}$$

with the weighted average $\bar{u}_r = \sum_{s=1}^{m} w_r^s u_r^s / \sum_{s=1}^{m} w_r^s$. This expression now explicitly shows how the receiver-satellite unit direction vectors and their corresponding satellite elevation weighting contribute to the variance matrix.

Height-Constrained Model

As we will see in the following, there are situations for which the IRNSS SPP model turns out to be too weak to provide accurate positioning. Height-constraining of the model would then be a possible remedy. Information on the height component could be provided if the vertical user position would be known on average and not vary too much. Examples of such applications are marine positioning, bathymetric surveying, and kinematic positioning over small areas with low height fluctuations (Zhu and Santerre 2002; Godha and Cannon 2007). When enforcing the weighted height constraint, the observational model in (1) is extended with

$$E\{\delta h\} = [0,\ 0,\ 1]\,\Delta x_r \ \ ,\ \ D\{\delta h\} = \sigma_h^2 \qquad (5)$$

in which δh denotes the height constraint corrected for an initial height value and σ_h is the a priori standard deviation of the height constraint.

3 IRNSS PDOP-HDOP Analysis

In this section we provide a single-point positioning dilution of precision analysis for a grid of locations covering IRNSS's two service areas.

Horizontal Dilution of Precision

We use the DOP as a scalar measure to diagnose the strength of the receiver-satellite geometry. The Position DOP (PDOP) is defined as (Teunissen 1998, Hofmann-Wellenhof et al. 2013)

$$\mathrm{P}DOP = \mathrm{trace}\left([G_r^T W_D G_r]^{-1}\right)^{0.5} = \frac{1}{\sigma}\mathrm{trace}(Q_{\hat{x}_r\hat{x}_r})^{0.5} \qquad (6)$$

The PDOP considers the impact of the receiver-satellite geometry on all three receiver coordinates. The Horizontal DOP (HDOP) is obtained in case only the horizontal receiver coordinates are considered.

In the following we provide the 24-hour PDOP and HDOP time series for different locations over the two service areas. As the IRNSS receiver-satellite geometry repeats itself every day four minutes earlier w.r.t the previous day, the signatures of these time series are representable for any day. Figure 2 shows the selected locations, for the primary service area in *red* and for the secondary service area in *black*.

Primary Service HDOP

Figure 3 shows the time series of the number of visible satellites (*black*), the PDOP (*red*) and the HDOP (*blue*) for the primary service area locations (see Figure 2). It can be seen that the PDOP and HDOP values are reasonably constant over the day for the locations at latitudes of 0° and 20°, with PDOP ≈ 4 and HDOP ≈ 2.

For locations (φ = 40°, λ = 65°) and (φ = 40°, λ = 101°) we note a difference in satellite visibility, despite their symmetry w.r.t. the location of satellite I3. This is due to the fact that the distribution of the other four IGSOs and two GEOs is not symmetric w.r.t the I3 location. For example, I6 is located 50.5° to the West of I3 whereas I7 is located 46.5° to the East of I3. Therefore, location (φ = 40°, λ = 65°) has a longer visibility of I7 than location (φ = 40°, λ = 101°) has of I6. Still, except for a distinct peak in the PDOP time series of location (φ = 40°, λ = 101°) over the period UTC [17:32:00-19:23:00], the PDOP and HDOP values are comparable to those of locations (φ = 40°, λ = 65°) and (φ = 40°, λ = 83°), with PDOP ≈ 6 and HDOP ≈ 4.

The occurrence of the PDOP peak at location (φ = 40°, λ = 101°) can be explained through the corresponding receiver-satellite geometry. Figure 4 depicts the satellites skyplot at UTC 18:30:30, which is the moment the PDOP peak occurs at location (φ = 40°, λ = 101°). It can be seen that at this moment in time the receiver-satellite line-of-sight unit vectors of all five satellites I1, I3, I4, I5 and I7 form a cone-like geometry (Teunissen 1990, Zaminpardaz et al. 2016), thus leading to a near rank-defect SPP design matrix and hence large PDOP values. Note that the poorest estimable direction, i.e. the direction of the cone symmetry axis, has almost no component in the horizontal plane. This explains why the large peak in the PDOP at location (φ = 40°, λ = 101°) (see Figure 3) is absent from the HDOP.

Secondary Service HDOP

Figure 5 shows the time series of the number of visible satellites (*black*), the PDOP (*red*) and the HDOP (*blue*) for the secondary service area locations (see Figure 2). When we consider the behavior of the DOP-values, four different categories of locations can be discriminated: **I**, **II**, **III** and **IV**.

For the locations in category **I**, the DOP-values are almost constant and similar to those of the primary service area, PDOP ≈ 4 and HDOP ≈ 2.5. Also the DOP-values of the locations within category **II** are reasonably constant, although somewhat more irregular than those of **I**. The first time that we really see a PDOP-peak occurring is at the locations of category **III**, the explanation of which is the same as given for primary service area location (φ = 40°, λ = 101°). More frequent and more extreme DOP-values, both for PDOP and HDOP, occur when we go to the border of the secondary service area at locations inside category **IV**. At these locations proper positioning is really becoming troublesome.

The large DOP-values at the border locations can be mitigated by imposing a height constraint (cf. 5). In Figure 6, the height-constrained ($\sigma_h / \sigma = 1$), practically coinciding PDOP and HDOP time series are presented for border locations in category **IV**. It can be seen that upon constraining the height component, non-equator locations indeed obtain a reasonably smooth DOP behavior for the whole 24-hour period. However, for the equator locations, there still exist two time intervals over which the height-constrained DOP reaches large values. This is due to the fact that at these two locations only four satellites, two GEOs and two IGSOs, are visible and therefore there are two periods when the two IGSOs occupy (almost) the same skyplot position, thus leading to a poor receiver-satellite geometry with corresponding large DOP values.

Day-Averaged HDOP Map

With the above given insight into the daily PDOP and HDOP behavior of the selected locations in the primary and secondary service areas, we now present a more fluid representation of the spatial HDOP variability. Figure 7 shows the 24-hour average IRNSS HDOP color map over its service areas. As the IRNSS receiver-satellite geometry repeats itself approximately every day, this average HDOP map can be considered a useful day-average. When using this value as an approximation to the actual HDOP, one should keep in mind though that this approximation will be poorer for locations that show a greater HDOP time-variability, such as when one gets closer to the borders of the secondary service area. The map can be used to compute the average horizontal positioning standard deviation for a particular location l as

$$\bar{\sigma}_l = \frac{\sigma}{\sqrt{2}}\overline{\mathrm{HDOP}_l} \tag{7}$$

in which $\overline{\mathrm{HDOP}_l}$ denotes the average HDOP value of that location.

4 IRNSS SPP Precision

In this section an overview is provided of the expected IRNSS's single-point positioning precision over the two service areas.

SPP Scatterplots and Confidence Ellipses

To get a first impression of the SPP repeatability, we have processed five days of 30-second IRNSS data collected with the cut-off elevation angle of 10° at two different stations in Western Australia. The two stations are Perth (φ = -32°, λ = 115.89°) and Fitzroy (φ = -18.13°, λ = 125.80°) which are equipped with JAVAD TRE_G3TH_8 receiver and SEPTENTRIO POLARX5 receiver, respectively. Perth is close to location (φ = -30°, λ = 115.5°) of the secondary service area, while Fitzroy is east of location (φ = -15°, λ = 115.5°) and close to the border of the secondary service area. The data are a priori corrected for the ionospheric delays using the predicted Global Ionosphere Map GIM (CODE 2016) and for the dry tropospheric delays using the Saastamoinen model (Saastamoinen 1972). Their user range accuracies were determined as $\sigma = 1.80\,\mathrm{m}$ for Perth and $\sigma = 2.30\,\mathrm{m}$ for Fitzroy by means of variance component estimation (VCE) (Teunissen and Amiri-Simkooei, 2008). For the relatively crude pseudorange-only SPP model, these estimates will include all remaining unmodelled effects, such as e.g., satellite orbital errors, satellite clock errors and residual atmospheric delays. That of Fitzroy is somewhat larger due to the additional ionospheric uncertainty. The single-epoch SPP scatterplots of the two stations are shown in Figure 8 (a and c). Superimposed on the scatterplots are also shown the formal (*green*) and empirical (*red*) 95% confidence ellipses, which show a reasonable good agreement. But note that the two SPP scatterplots are not as homogeneous as one would expect if data would be coming from a normal distribution. The reason for this lack of homogeneity lies in the presence of mismodelled effects, particularly due to the satellite clocks and ionospheric delays. These effects would be absent if one would consider relative point positioning (RPP) between two nearby stations. This is demonstrated in Figure 8 (b) which shows the RPP scatterplot of Perth and a closeby station.

Note that the Fitzroy scatterplot is far more elongated than the one of Perth (Figure 8, a and c). This is due to the relatively poor receiver-satellite geometry of Fitzroy, being so close to the border of the secondary service area. Considerable improvement is possible though if one applies a height constraint. Figure 8 (d) shows the Fitzroy scatterplot when a height constraint of $\sigma_h = 1\,\text{m}$ is applied.

Also note that all confidence ellipses of Figure 8 are oriented in a north-westerly direction. This can be explained by means of the receiver-satellite geometry and its impact on the confidence ellipse of $\hat{x}_r$,

$$(\hat{x}_r - x_r)^T Q^{-1}_{\hat{x}_r\hat{x}_r} (\hat{x}_r - x_r) = r^2 \tag{8}$$

in which the constant r^2 is chosen such that a certain confidence level is reached. As the direction of elongation is given by the direction of the eigenvector of $Q^{-1}_{\hat{x}_r\hat{x}_r}$ corresponding to its smallest eigenvalue, it follows with the aid of (4) that this direction is given by

$$\begin{aligned} f &= \arg\min_{\tilde{f}} \; \tilde{f}^T Q^{-1}_{\hat{x}_r\hat{x}_r} \; \tilde{f} \\ &= \arg\min_{\tilde{f}} \sum_{s=1}^{m} w_r^s \, [\, \tilde{f}^T (u_r^s - \bar{u}_r)]^2 \end{aligned} \tag{9}$$

Figure 9 depicts the day-averaged skyplot position of the IRNSS satellites as well as that of the weighted-average $\bar{u}_r$ at Perth on DOY 153 of 2016 with cut-off angle of 10°. As the differences $(u_r^s - \bar{u}_r)$ are mainly oriented along the North-East direction, the direction f that minimizes their contribution to (9) will mainly lie in a North-Westerly direction.

Primary service area

We now provide an overview of the SPP precision for the primary service area. Table 2 gives for the primary service area locations (within the *gray* box), the day-averaged values of their North and East standard deviations, σ_N and σ_E, and corresponding correlation coefficients ρ_{NE}. For each location, there are two rows of values; the first row corresponds to the unconstrained scenario with $\sigma = 1$m while the second row to the height-constrained scenario with $\sigma = 1$m and $\sigma_h / \sigma = 1$. Given the user range accuracy of $\sigma = 1$m, the rate of change of the horizontal precision w.r.t. the variation of the ratio σ_h / σ can be described considering two cases $\sigma_h / \sigma > 1$and $\sigma_h / \sigma < 1$. The average rate of change of the horizontal precision w.r.t. $\sigma_h / \sigma > 1$ is zero for the locations within (-30° <φ < 40°, 65° <λ < 110°), 0.01, 0.25, 0.14, 0.43 and 0.22 for the locations within (λ = 50.5°, 115.5°), (φ < 40°, λ = 30°), (φ < 40°, λ = 130°), (φ = 40°, λ = 30°) and (φ = 40°, λ = 130°), respectively. The average rate of change of the horizontal precision w.r.t. $\sigma_h / \sigma < 1$is 0.07, 0.03, 0.02, 0.02, 0.02, 0.04 and 0.06 for the locations on (λ = 30°, 50.5°, 65°, 83°, 110°, 155.5° and 130°), respectively. For any other values of user range accuracy σ, one can scale these rates of change and the results in Table 2 accordingly. For example, for $\sigma = 3$m, these values should be multiplied by 3. The table-values can be considered representative for the whole day as their HDOP time series showed a rather stable behavior over the 24-hour period, see Figure 3.

It follows from Table 2 that location (φ = 0°, λ = 83°), being the ground tracks symmetry point, has the best precision and that the precision gets poorer in north/south direction the further one departs from the equator and likewise poorer in east/west direction the further one moves away from this location in such east/west direction. As the impact of height-constraining is larger the poorer the unconstrained precision, its effect is felt more the further one is from location (φ = 0°, λ = 83°). But overall the effect of height-constraining on these primary service area locations is only marginal.

Secondary Service area

We now provide an overview of the SPP precision for the secondary service area. Table 2, outside the *gray* box, gives an overview for the secondary service area locations. All the day-averaged entries of the table can be considered representative for the whole day as their corresponding HDOP time series are shown to be sufficiently stable, see Figure 5. Note that the formal results given for location (φ = -30°, λ = 115.5°), which is close to Perth, is indeed consistent with the empirical results obtained for Perth (Figure 8 a).

As was mentioned for the primary service area locations, the results of the secondary service area show the general tendency that the SPP precision gets poorer the further one moves away from the central location (φ = 0°, λ = 83°). However, for the locations on the border of the secondary service area, with longitudes of λ = 30°, 130°, the worsening in the SPP precision is such that no representative day-average can be given. As their unconstrained HDOP-values show very large excursions over the day (cf. Figure 5), no day-averaged values have been given for these locations in Table 2. For their height-constrained case the situation is different. Upon constraining the height component, the HDOP time series at locations with latitudes of φ = -30°, 30°, 40° almost flatten and the corresponding day-averaged precision can be considered representative again (cf. Figure 6). This is however not the case for the equator and near-equator locations with latitudes of φ = -15°, 0°, 20°. Their height-constrained day-averaged values are therefore excluded from Table 2. To have a better description of their precision, we divided the 24-hour period into two sub-periods; one sub-period accommodating the large peaks for the HDOP and one containing the remaining part of the 24-hour period (cf. Figure 6). Note that these sub-periods are similar for locations with the same longitude. Table 3 lists the average North, East standard deviations and correlation coefficients for these locations over the sub-periods with smooth HDOP behavior.

The East-North correlation coefficients given in Tables 2 and 3 show that for those locations with the same longitude or the same latitude of central location (φ = 0°, λ = 83°) of primary service area, East and North components can be considered uncorrelated. Comparing the East and North standard deviations for these locations, it can be said that their corresponding horizontal confidence ellipses are vertically or horizontally elongated towards location (φ = 0°, λ = 83°) of primary service area. For the locations with different latitude and longitude from those of location (φ = 0°, λ = 83°) of primary service area, the East-North correlation is such that their corresponding confidence ellipses are elongated towards this point.

Finally we note, although the above tables provide day-averaged values, while the IRNSS satellite ground tracks do not exactly have a 24-hour repeat cycle, that the values provided can still be considered representative for any arbitrary day. The unconstrained mean values given in Tables 2 and 3 can vary for any other arbitrary day by at most 2 cm in North and 4 cm in East for the user range accuracy of σ=1m. Theses variations get smaller when the underlying model is strengthened by a weighted height constraint. Irrespective of the value of σ_h, the largest variation in the mean North and East standard deviations is 1 cm in case σ=1m.

5 Summary and Conclusions

As IRNSS has recently (May 2016) become operational, it is important to gain an understanding of its navigational potential and actual positioning capabilities for civilian users. This contribution has provided for that purpose a first full constellation IRNSS single-point positioning precision analysis over its two service areas. A dilution of precision analysis of daily PDOP and HDOP time series was given, including the identification, in location and time, of poor receiver-satellite geometries. The nature of these geometries was explained and it was demonstrated how the impact of some of these poor receiver-satellite geometries can be mitigated by means of height-constraining. We also provided an overview and analysis of the single-point positioning precision for a grid of locations covering the two service areas. It includes, with the exception of six locations, easy-to-use representative day-averaged values of the positioning precision, unconstrained as well as height-constrained. For the six exempted locations, on and near the equator on the border of the secondary service area, sub-day averages were given.

Acknowledgements

The second author is the recipient of an Australian Research Council (ARC) Federation Fellowship (project number FF0883188). A part of the IRNSS date was provided by Geoscience Australia. This support is gratefully acknowledged.

References

Babu R, Mula P, Ratnakara SC, Ganeshan AS. 2015. “IRNSS satellite parameter estimation using combination strategy.” *Global Journal of Science Frontier Research*, 15(3): 87–95.

Chandrasekhar MV, Rajarajan D, Satyanarayana G, Tirmal N, Rathnakara SC, Ganeshan AS. 2015. “Modernized IRNSS broadcast ephemeris parameters.” *Control Theory and Informatics*, 5(2): 1–9.

CODE. 2016. “Global ionosphere maps produced by CODE.” Accessed July 2016. ftp://ftp.unibe.ch/aiub/CODE/2015.

Euler HJ, Goad CC. 1991. “On optimal filtering of GPS dual frequency observations without using orbit information.” *Bulletin Geodesique* 65(2):130–143.

Ganeshan AS. 2012. “Overview of GNSS and Indian Navigation Program”. Paper presented at GNSS User Meeting, ISRO Satellite Center, Bangalore, Februery 23.

Ganeshan AS, Ratnakara SC, Srinivasan N, Rajaram B, Tirmal N, Anbalagan K. 2015. “First Position Fix with IRNSS.” *Inside GNSS*, July/August 2015. Accessed April 2016. http://www.insidegnss.com/node/4545.

Godha S, Cannon M. 2007. “GPS/MEMS INS integrated system for navigation in urban areas.” *GPS Solutions* 11(3):193–203.

Hofmann-Wellenhof B, Lichtenegger H, Collins J. 2013. *Global positioning system: theory and practice*. Springer Science & Business Media.

ISRO. 2014. “Indian regional navigation satellite system: signal in space ICD for standard positioning service, Version 1.0.” *ISRO Satellite Centre*, June 2014.

ISRO. 2016. “PSLV-C33/IRNSS-1G.” Accessed July 2016. http://www.isro.gov.in/sites/default/files/pslv-c33-brochure.pdf.

Kumari A, Samal K, Rajarajan D, Swami U, Babu R, Kartik A, Rathnakara SC, Ganeshan AS. 2015. “Precise modeling of solar radiation pressure for IRNSS satellite.” *Journal of Natural Sciences Research* 5(3), 35–43.

Montenbruck O, Steigenberger P, Riley S. 2015. “IRNSS orbit determination and broadcast ephemeris assessment.” Paper presented at International Technical Meeting of The Institute of Navigation, Dana Point, CA, January 26–28. pages 185–193.

Mozo Garcia A, Piriz R, Lainez Samper MD, Romay Merino MM. 2010. “Multisystem Real Time Precise-Point-Positioning, today with GPS+GLONASS in the near future also with

QZSS, Galileo, Compass, IRNSS.” Paper presented at International Symposium on GPS/GNSS, Taipei, Taiwan, October 26-28.

Nadarajah N, Khodabandeh A, Teunissen PJG. 2015. “Assessing the IRNSS L5-signal in combination with GPS, Galileo, and QZSS L5/E5a-signals for positioning and navigation.” *GPS Solutions,* 20:289-297.

Odijk D, Nadarajah N, Zaminpardaz S, Teunissen PJG. 2016. “GPS, Galileo, BDS, QZSS and IRNSS Differential ISBs: Estimation and Application.” *GPS Solutions*. Accessed July 2016. doi:10.1007/s10291-016-0536-y.

Pal S, Ganeshan AS.2015. “Indian GNSS Paradigm.” In *2015 PNT Symposium*. Standford, CA, 12-13 November 2015.

Rao VG. 2013. “Proposed LOS fast TTFF signal design for IRNSS.” PhD diss. University of Calgary.

Rethika T, Mishra S, Nirmala S, Rathnakara SC, Ganeshan AS. 2013. “Single frequency ionospheric error correction using coefficients generated from regional ionospheric data for IRNSS.” *Indian Journal of radio & Space Physics* 42(3), 125–130.

Saastamoinen J. 1972. “Atmospheric correction for the troposphere and stratosphere in radio ranging satellites.” In *The use of artificial satellites for geodesy,* edited by S.W. Henriksen, A. Mancini and B.H. Chovitz, 247–251. Washington, DC, American Geophysical Union.

Saikiran B, Vikram V. 2013. “IRNSS architecture and applications.” *Journal of Comm & Electron* 1(3): 21–27.

Sarma AD, Sultana Q, Srinivas VS. 2010. “Augmentation of indian regional navigation satellite system to improve dilution of precision.” *Journal of Navigation* 63(2): 313–321.

Sekar SB, Sengupta S, Bandyopadhyay K. 2012. “Spectral compatibility of BOC (5, 2) modulation with existing GNSS signals.” Paper presented at Position Location and Navigation Symposium (PLANS), 2012 IEEE/ION, IEEE. pages 886–890.

Su XL, Zhan XQ, Niu MC, Zhang YH. 2012. “Performance Comparison for Combined Navigation Satellite Systems in Asia-Pacific Region.” *Journal of Aeronautics, Astronautics and Aviation*. Series A 44(4):249-257.

Teunissen PJG. 1990. “GPS op afstand bekeken.” *In:* een halve eeuw in de goede richting. Lustrumboek Snellius 1985-1990, DUM Delft, 215–233.

Teunissen PJG. 1998. “A proof of Nielsen’s conjecture on the relationship between dilution of precision for point positioning and for relative positioning with GPS.” *IEEE on Aerospace and Electronic Systems* 34(2): 693–695.

Teunissen PJG, Amiri-Simkooei AR. 2008. “Least-squares variance component estimation.” *Journal of Geodesy* 82(2):65–82

Thoelert S, Montenbruck O, Meurer M. 2014. “IRNSS-1A: signal and clock characterization of the Indian regional navigation system.” *GPS solutions* 18(1): 147–152.

Thombre S, Bhuiyan MZH, Söderholm S, Kirkko-Jaakkola M, Ruotsalainen L, Kuusniemi H. 2016. “A Software Multi-GNSS Receiver Implementation for the Indian Regional Navigation Satellite System” *IETE Journal of Research* 62(2):246-256.

Zaminpardaz S, Teunissen PJG, Nadarajah N. 2016. “IRNSS stand-alone positioning: first results in Australia.” *Journal of Spatial Science* 61(1):5–27.

Zhu J, Santerre R. 2002. “Improvement of GPS phase ambiguity resolution using prior height information as a quasi-observation.” *Geomatica* 56(3):211–221.

Table 1 Information on the IRNSS satellites (ISRO 2016).

Satellite	Type	Longitude	Inclination	Launch date
IRNSS-1A (I1)	IGSO	55° E	29.0°	July 2013
IRNSS-1B (I2)	IGSO	55° E	31.0°	April 2014
IRNSS-1C (I3)	GEO	83° E	-	October 2014
IRNSS-1D (I4)	IGSO	111.75° E	30.5°	March 2015
IRNSS-1E (I5)	IGSO	111.75° E	28.1°	January 2016
IRNSS-1F (I6)	GEO	32.5° E	-	March 2016
IRNSS-1G (I7)	GEO	129.5° E	-	April 2016

Table 2 IRNSS L5 single-epoch SPP North-East formal standard deviations, σ_N , σ_E , and correlation coefficients, ρ_{NE} with the cut-off elevation angle of 10° over the IRNSS service area. There are two rows of values for each location; first row corresponds to the unconstrained scenario ($\sigma = 1$ m) and second row to the height-constrained scenario ($\sigma = 1$ m and $\sigma_h / \sigma = 1$). On each row, three values are given which are (from left to right) σ_N [m] , σ_E [m], ρ_{NE} . These values are the day-averaged values for DOY 153 of 2016. The *gray* box contains the results of the primary service area.

φ\λ	30°	50.5°	65°	83°	101°	115.5°	130°
40°	- 4.82,4.16,-0.73	4.58,2.49,-0.71 3.28,1.90,-0.57	3.57,1.52,-0.52 3.03,1.40,-0.42	3.41,1.21,0.00 3.02,1.19, 0.01	3.95,1.67, 0.58 3.08,1.47, 0.44	4.79,3.13, 0.74 3.30,2.08, 0.61	- 4.05,3.53, 0.68
30°	- 3.74,3.00,-0.55	3.53,2.16,-0.58 2.56,1.59,-0.47	2.66,1.29,-0.50 2.34,1.18,-0.38	2.56,0.98, 0.01 2.26,0.98, 0.01	2.86,1.42, 0.56 2.36,1.25, 0.40	3.62,2.71, 0.56 2.59,1.73, 0.50	- 3.19,2.72, 0.52
20°	- -	3.01,2.01,-0.41 2.28,1.44,-0.38	2.11,1.18,-0.42 1.94,1.04,-0.31	1.99,0.86, 0.01 1.80,0.86, 0.01	2.18,1.32, 0.48 1.94,1.09, 0.33	2.83,2.44, 0.47 2.27,1.56, 0.41	- -
0°	- -	2.16,1.93, 0.00 2.16,1.31, 0.00	1.65,1.12, 0.00 1.65,0.93, 0.00	1.49,0.78, 0.00 1.49,0.78, 0.00	1.63,1.26, 0.00 1.63,0.97, 0.00	2.11,2.31, 0.00 2.11,1.40, 0.00	- -
-15°	- -	2.50,1.97, 0.38 2.21,1.39, 0.31	1.92,1.15, 0.35 1.81,0.99, 0.25	1.78,0.82,-0.01 1.66,0.82, 0.00	1.95,1.29,-0.40 1.80,1.04,-0.26	2.47,2.37,-0.41 2.19,1.49,-0.33	- -
-30°	- 3.77,3.01, 0.55	3.56,2.15, 0.58 2.56,1.59, 0.48	2.66,1.29, 0.50 2.34,1.18, 0.39	2.56,0.98,-0.01 2.26,0.98,-0.01	2.86,1.42,-0.56 2.36,1.24,-0.41	3.59,2.71,-0.56 2.58,1.73,-0.51	- 3.18,2.71,-0.53

Table 3 IRNSS L5 single-epoch SPP North-East formal standard deviations, σ_N, σ_E, and correlation coefficients, ρ_{NE} with the cut-off elevation angle of 10° on the IRNSS secondary service area border (see Figure 3). These values are the day-averaged values (excluding the mentioned periods) for DOY 153 of 2016 for height-constrained scenario ($\sigma = 1\,\mathrm{m}$ and $\sigma_h / \sigma = 1$).

φ	**λ**	**24-hour period excluding two sub-periods (UTC [hh:mm])**	σ_N **[m] ,** σ_E **[m],** ρ_{NE}
20°	30°	[09:00–11:41] & [20:56–23:17]	2.47,2.48,-0.32
20°	130°	[05:40–07:38] & [17:50–19:23]	2.41,2.30, 0.31
0°	30°	[09:12–11:25] & [21:11–23:23]	2.15,2.23, 0.01
0°	130°	[05:01–07:35] & [17:26–19:32]	2.05,2.12, 0.00
-15°	30°	[09:06–11:29] & [21:04–23:31]	2.31,2.36, 0.24
-15°	130°	[05:47–07:24] & [17:37–19:31]	2.29,2.21,-0.23

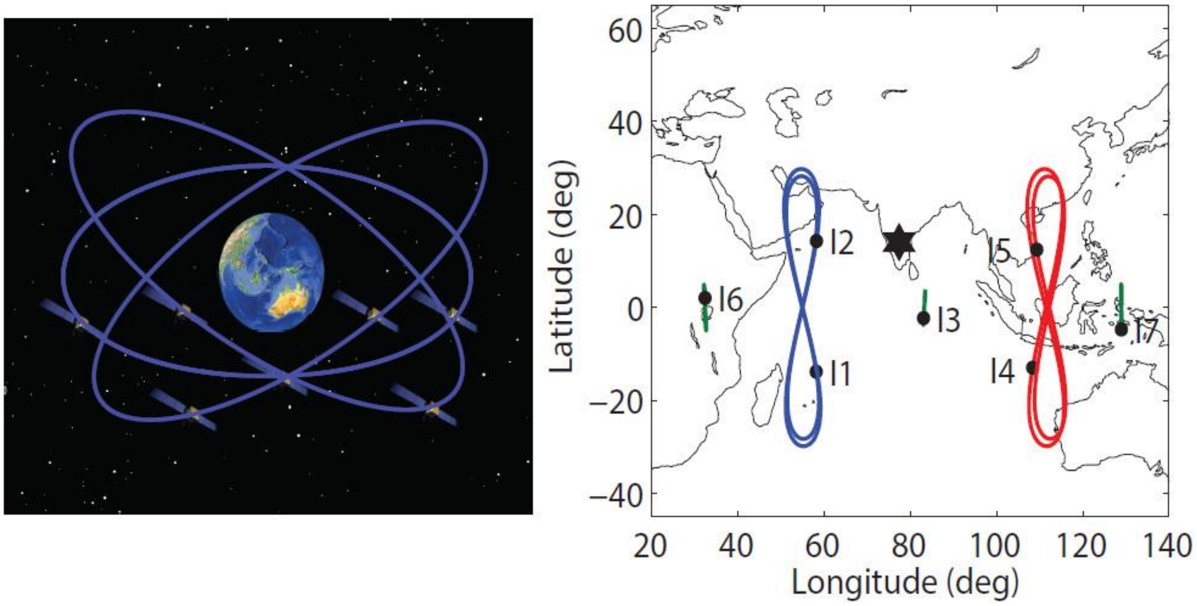

Figure 1. (Left) The 7 satellite IRNSS constellation. (Right) The 3 GEO and 4 IGSO satellite ground tracks of IRNSS.

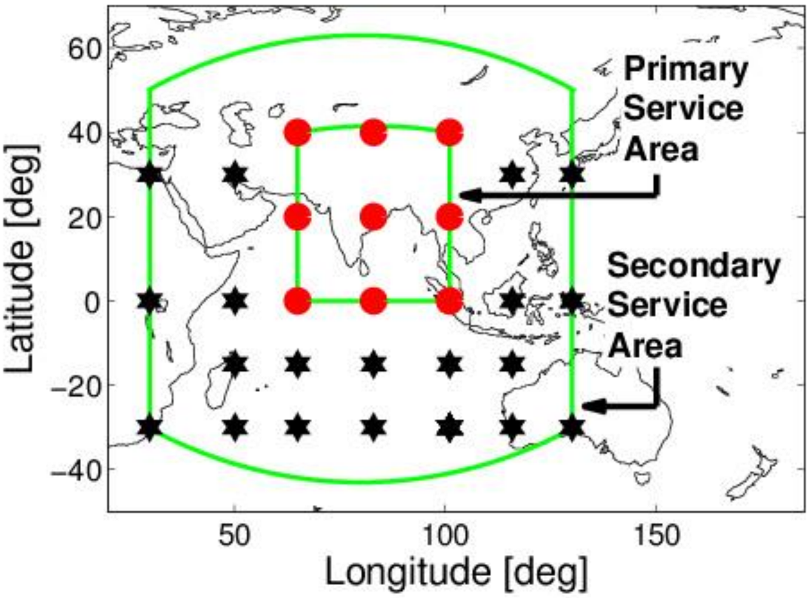

Figure 2. Primary (*red*) and secondary (*black*) service area locations. The inner and outer *green* boundaries indicate the border of the primary and secondary service areas, respectively.

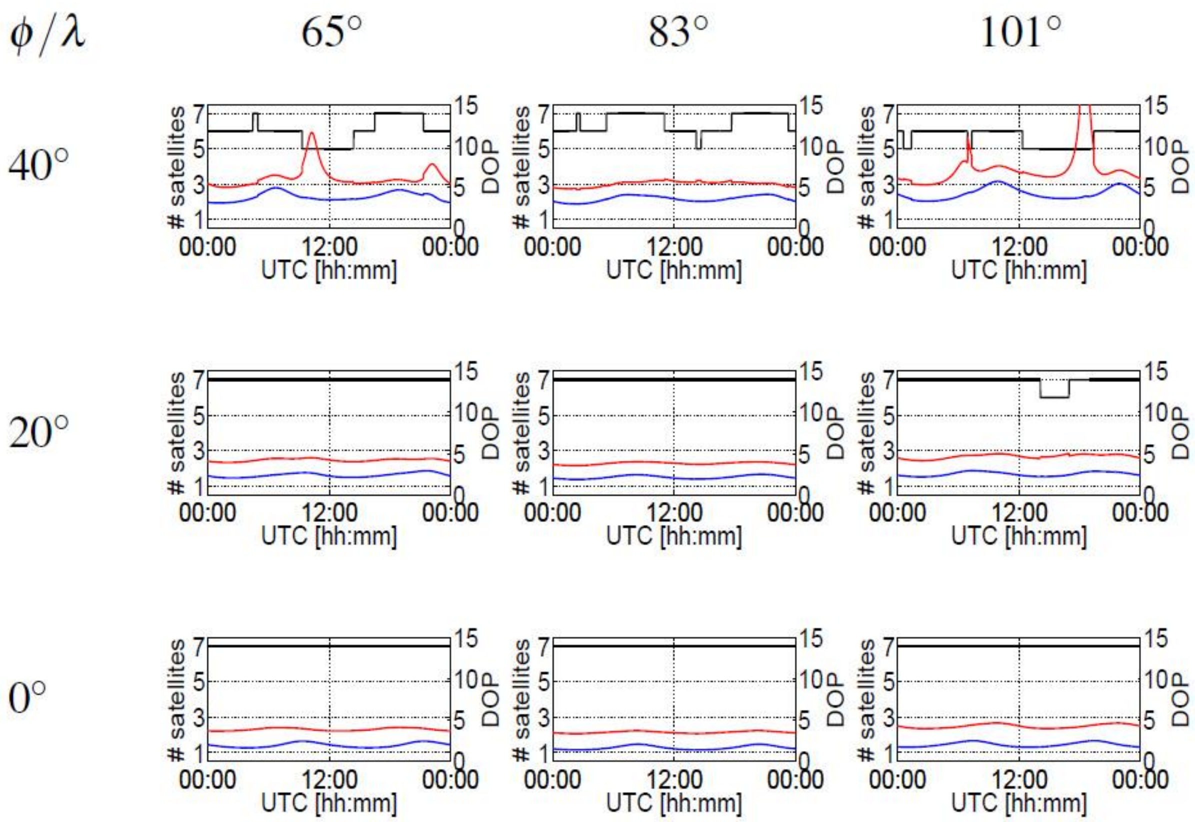

Figure 3. Primary service area time series of the number of visible IRNSS satellites (*black*) on DOY 153 of 2016, with 10° cut-off angle, and the corresponding PDOP (*red*) and HDOP (*blue*) values.

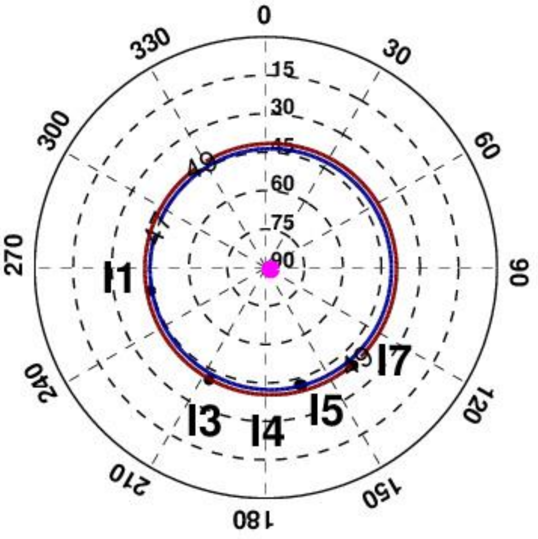

Figure 4. IRNSS satellites skyplot at UTC 18:30:30 of primary service area location (φ = 40°, λ = 101°) on DOY 153 of 2016, with 10° cut-off angle. The circles and the straight lines are the axes for the elevation and azimuth, respectively. The cone symmetry axis (poorest estimable direction) is identified by the *purple* dot and the circular contour lines show the loci of the directions that make angles of 47° and 49° with this symmetry axis.

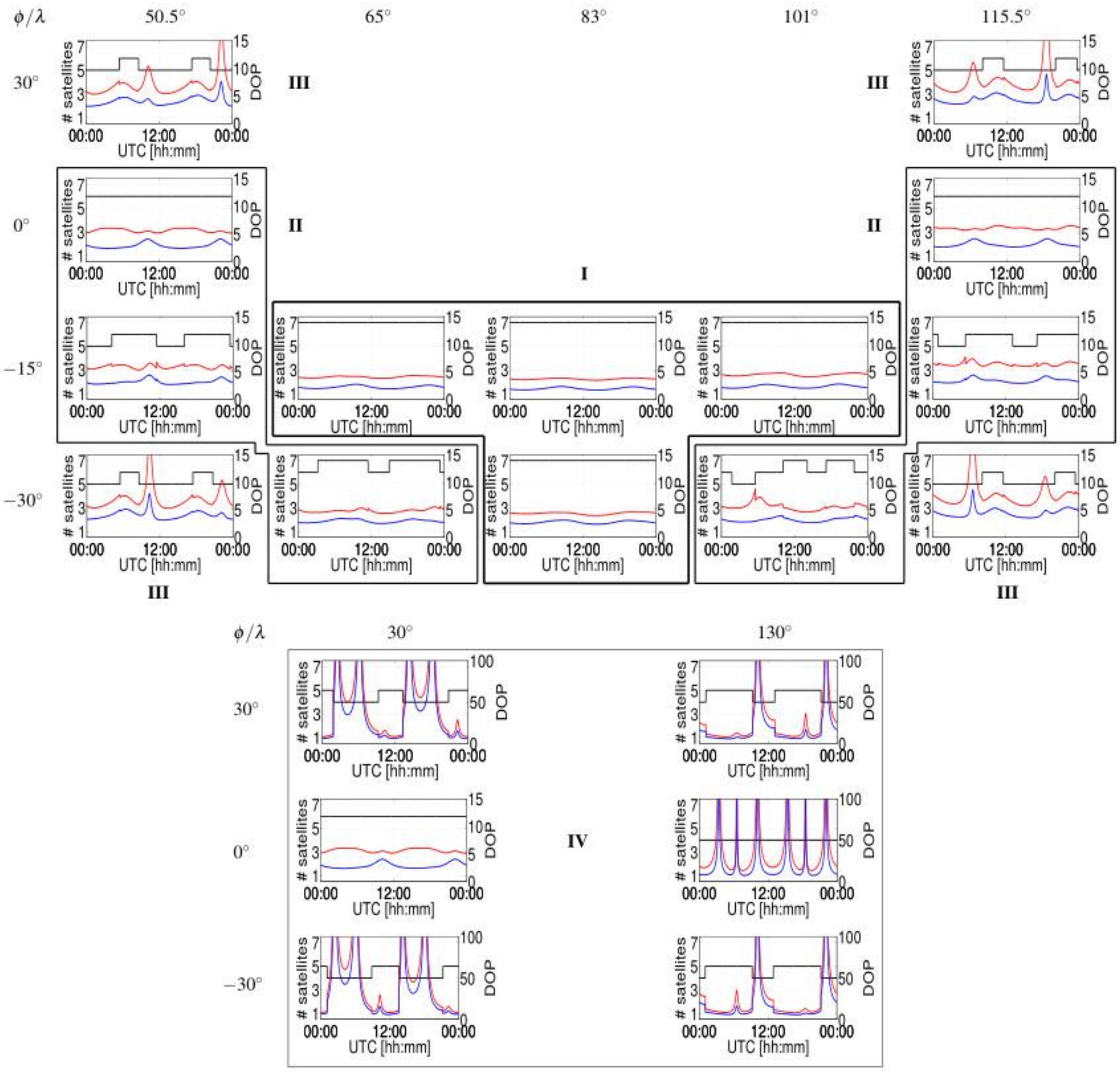

Figure 5. Secondary service area time series of the number of visible IRNSS satellites (*black*) on DOY 153 of 2016, with 10° cut-off angle, and the corresponding PDOP (*red*) and HDOP (*blue*) values.

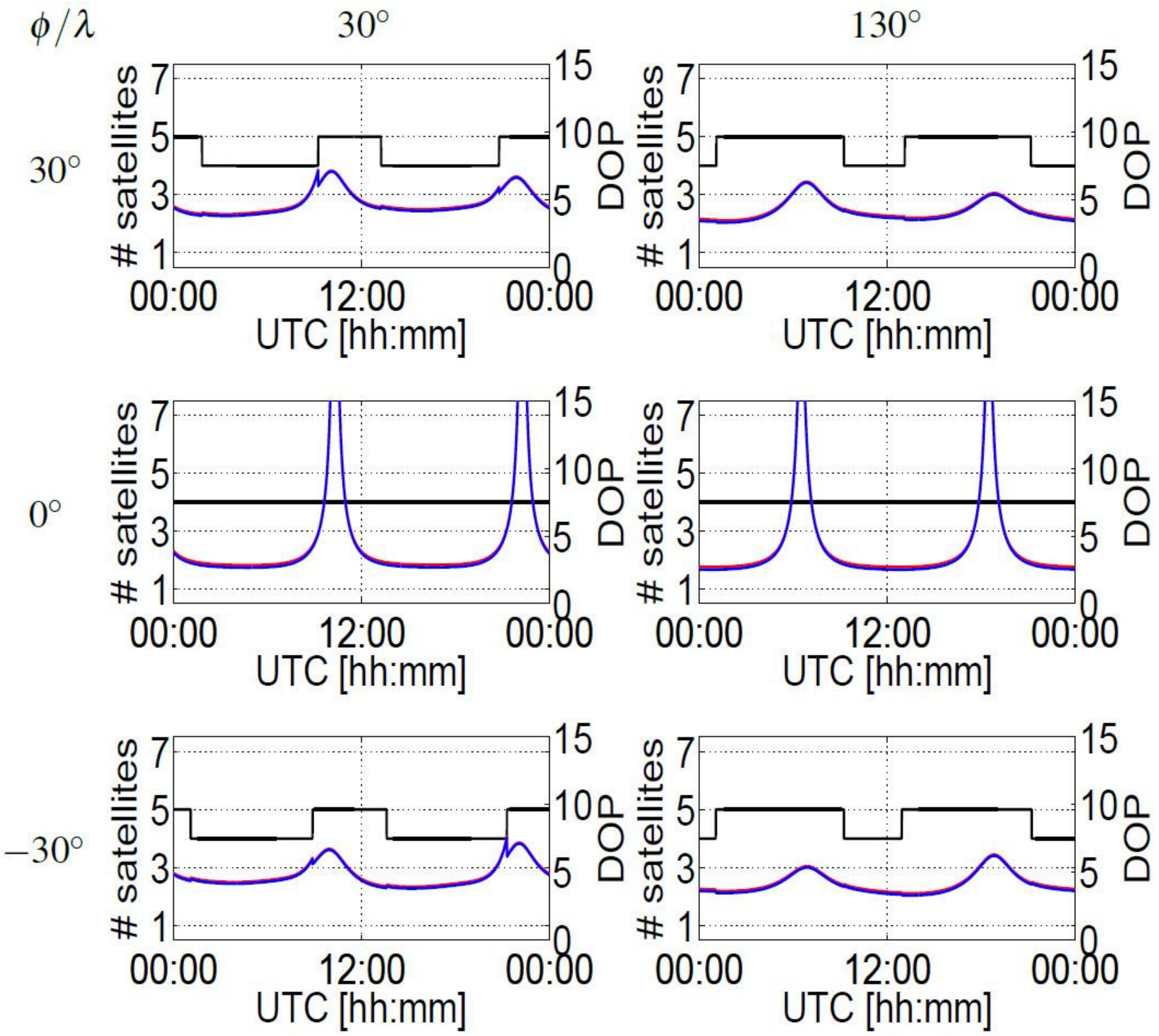

Figure 6. Time series of the number of visible IRNSS satellites and the corresponding height-constrained PDOP (*red*) and HDOP (*blue*) with $\sigma_h / \sigma = 1$ over the secondary service area, on DOY 153 of 2016 with 10° cut-off angle.

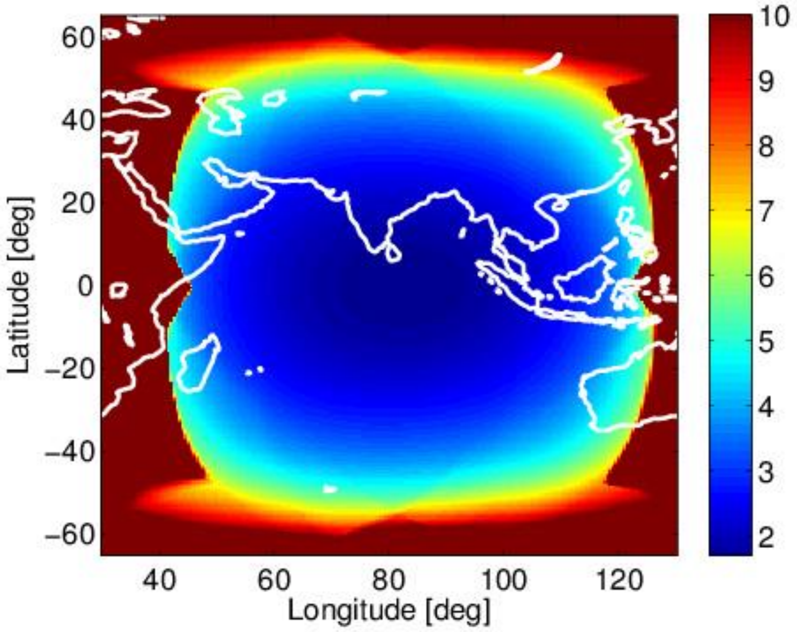

Figure 7. Day-averaged IRNSS HDOP color map for DOY 153 of 2016 with 10° cut-off angle.

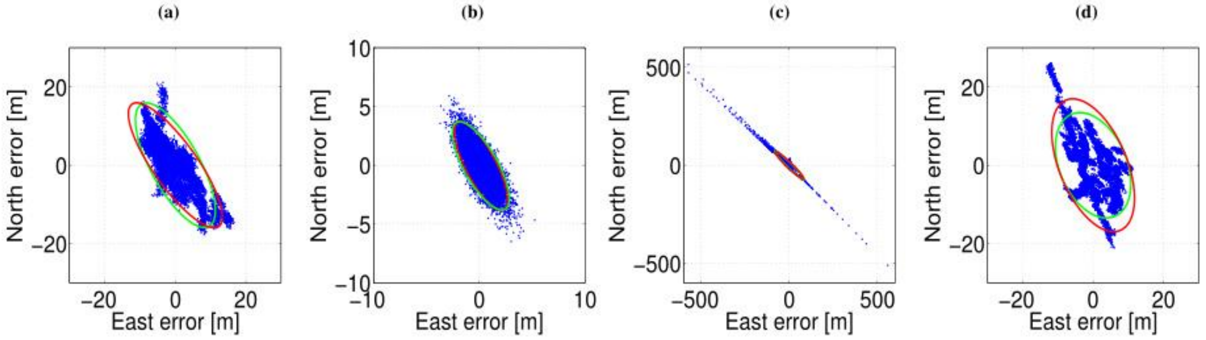

Figure 8. Single-epoch (30-sec sampling rate) scatterplots for five DOYs of 2016 with 10° cut-off angle. Formal (*green*) and empirical (*red*) 95% confidence ellipses are also shown. (a) Perth SPP scatterplot (close to location (φ = -30°, λ = 115.5°) of secondary service area); (b) Perth RPP scatterplot; (c) Fitzroy SPP scatterplot (east of location (φ = -15°, λ = 115.5°) close to border of secondary service area); (d) Fitzroy height-constrained SPP scatterplot ($\sigma_h = 1\text{m}$).

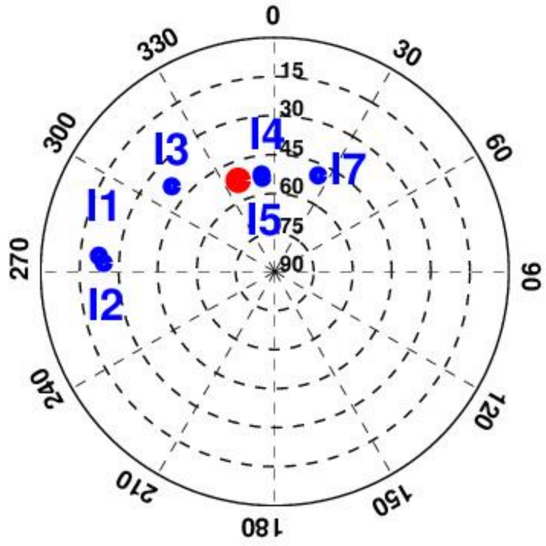

Figure 9. Day-averaged IRNSS skyplot at Perth for DOY 153 of 2016 with 10° cut-off angle. The circles and the straight lines are the axes for the elevation and azimuth, respectively. The *red* circle indicates the skyplot position of vector $\bar{u}_r$.